



Interfacial Polygonal Nanopatterning of Stable Microbubbles

Emilie Dressaire, *et al.*
Science **320**, 1198 (2008);
DOI: 10.1126/science.1154601

The following resources related to this article are available online at www.sciencemag.org (this information is current as of May 30, 2008):

Updated information and services, including high-resolution figures, can be found in the online version of this article at:

<http://www.sciencemag.org/cgi/content/full/320/5880/1198>

Supporting Online Material can be found at:

<http://www.sciencemag.org/cgi/content/full/320/5880/1198/DC1>

This article **cites 25 articles**, 2 of which can be accessed for free:

<http://www.sciencemag.org/cgi/content/full/320/5880/1198#otherarticles>

This article appears in the following **subject collections**:

Physics, Applied

http://www.sciencemag.org/cgi/collection/app_physics

Information about obtaining **reprints** of this article or about obtaining **permission to reproduce this article** in whole or in part can be found at:

<http://www.sciencemag.org/about/permissions.dtl>

Interfacial Polygonal Nanopatterning of Stable Microbubbles

Emilie Dressaire,¹ Rodney Bee,² David C. Bell,¹ Alex Lips,² Howard A. Stone^{1*}

Micrometer-sized bubbles are unstable and therefore difficult to make and store for substantial lengths of time. Short-term stabilization is achieved by the addition of amphiphilic molecules, which reduce the driving force for dissolution. When these molecules crystallize on the air/liquid interface, the lifetime of individual bubbles may extend over a few months. We demonstrated low gas-fraction dispersions with mean bubble radii of less than 1 micrometer and stability lasting more than a year. An insoluble, self-assembled surfactant layer covers the surface of the microbubbles, which can result in nanometer-scale hexagonal patterning that we explain with thermodynamic and molecular models. The elastic response of the interface arrests the shrinkage of the bubbles. Our study identifies a route to fabricate highly stable dispersions of microbubbles.

In two-phase systems, such as foams, emulsions, pastes, and dispersions, the structures of the dispersed and continuous phases play a critical role in determining the properties of the material (*1*). Correlations have been established between the properties and the size, shape, volume fraction, spatial distribution, and connectivity of the dispersed phase (*2–4*). The metastability of these two-phase systems adds time dependence to this list of complex functions: The microstructure of the dispersed phase continuously evolves toward lower-energy configurations by minimizing the interfacial area, which diminishes the long-term usefulness of two-phase systems. The development of models predictive of the time evolution during coarsening (*5, 6*) and of slowly aging systems with jammed interfaces (*7, 8*) are among the approaches used to overcome this limitation.

The most important and rapid coarsening occurs in gas-liquid two-phase systems with fine structuring (1 to 10 μm), such as contrast agents for ultrasound imaging, aerated food and personal care products, and foamed construction materials (*9–11*). Because the air/liquid surface tension produces a pressure that drives bubble dissolution by gas diffusion into the liquid phase, the initial structure evolves and larger bubbles grow at the expense of smaller ones (Ostwald ripening). The time scale of this separation prevents the preparation of bubbles in the colloidal range because a micrometer-sized bubble dissolves in less than 1 s in pure water (*12*). The lifetime can be increased to hundreds of seconds by the addition of surfactant molecules that lower the interfacial tension and decrease the pressure difference (*13*). Further improvements in stabilization have been achieved by coating the air/liquid interface with ordered nanoparticles (*8, 14*) or with gelled lipids (*15–17*); isolated bubbles with radii mostly greater than 10 μm were stable over a period of a few months.

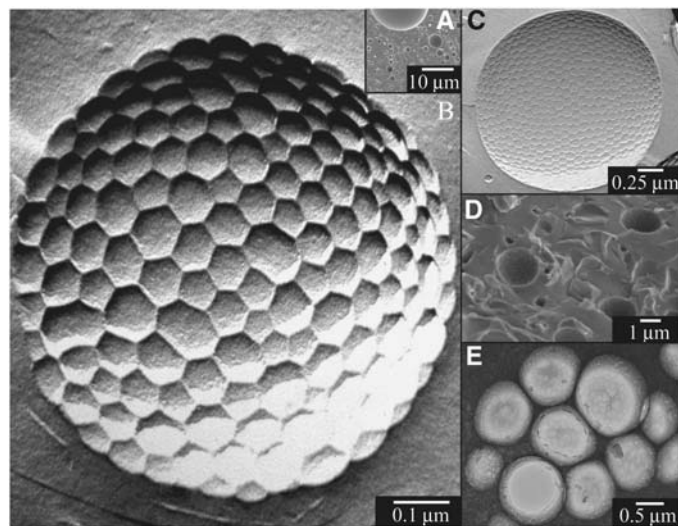
¹School of Engineering and Applied Sciences, Harvard University, Cambridge, MA 02138, USA. ²Unilever Research and Development, 40 Merritt Boulevard, Trumbull, CT 06611, USA.

*To whom correspondence should be addressed. E-mail: has@seas.harvard.edu

We report very stable gas dispersions obtained using a standard multiphase mixing technique to trap air into surfactant shells within a viscous bulk phase (*18*). The surfactant solution was prepared by mixing at 70°C a highly viscous glucose syrup [75 weight percent (wt %)] with water (23 wt %) and sucrose stearate as the surfactant (2 wt %; principally a mixture of mono- and diesters). The formation of the dispersion was achieved by aeration, via shearing, at room temperature for 2 hours. The mechanical entrainment of air was followed by comminution; that is, the reduction in bubble size by shear-induced breakup.

The gas phase, which occupies about half the volume of the resulting foam (gas volume fraction ~ 0.45), is divided into surfactant-covered bubbles, or gas microcells, whose size ranged from

Fig. 1. Low gas-fraction dispersion of microbubbles with nanotextured surfaces. **(A)** Cryo-SEM image of the dispersion produced by shearing the surfactant mixture for 2 hours at a shear rate $\dot{\gamma} \approx 475\text{s}^{-1}$. The highly polydisperse population of bubbles is characterized by radii ranging between hundreds of nanometers and tens of micrometers. **(B)** TEM image of a micrometer-sized bubble covered with hexagons ~ 50 to 100 nm in diameter. The platinum shadowing of the surface replica, under a 45° angle, reveals that the domains are buckled outward. **(C)** TEM image of a microbubble (radius $R_b \approx 1.5\ \mu\text{m}$). The surface structure is regular both in shape (mostly hexagons) and in size ($\sim 50\ \text{nm}$); it includes a distribution of heptagons and pentagons. Patterns may look distorted because they sit on a curved interface. **(D)** Cryo-SEM image of the bubbles. The three-dimensional structuring of the air/glucose syrup interface appears on all of the micrometer-sized bubbles. **(E)** Cryo-TEM image of bubbles. The plunge freezing leads to nonspherical shapes. The electron beam partially melts the surfactant layer, which enables direct visualization of the hollowness of the bubbles.



hundreds of nanometers to tens of micrometers (Fig. 1A). The majority of the bubbles have radii R_b of about 1 μm and are characterized by a regular nanometer-scale structuring: Hexagonal domains that buckle outward from the bubble fully cover the air/liquid interface (Fig. 1B). These features were best observed with freeze-fracture transmission electron microscopy (TEM), as illustrated in Fig. 1C. A distribution of pentagons and heptagons disturb the lattice, which had typical dimensions such as scale $\sim 50\ \text{nm}$. The pattern is not an imaging artifact or an isolated phenomenon because large bubble populations have been screened by cryogenic scanning electron microscopy (cryo-SEM), showing that the structure is systematically visible on these microbubbles (Fig. 1D) and can appear on larger ones. We characterized the inner bubble structure by cryo-TEM (Fig. 1E). Direct imaging induces a partial melting of the air/liquid interface, which reveals a spherical gas-filled cavity [supporting online material (SOM) text and fig. S1]. Taken together, the images of Fig. 1 provide evidence that, in this system, every microbubble has a nanometer-scale, nearly hexagonal surface pattern. Individual bubbles with some similar qualitative interfacial characteristics, but lacking regularity, have been observed in phospholipid-coated systems (*16, 17*).

We describe here the dependence of the pattern size and the bubble radius on the processing conditions. Results were obtained by analyzing a few tens of TEM micrographs of freeze-fracture replicas for each dispersion (*18*). By sampling the mixture at different times during the aeration process, the evolution of the radii of the bubbles and the domains were monitored (SOM text and fig. S2). Figure 2, A and B, shows the

evolution of the mean bubble and domain radii upon shearing and subsequent storage over a 45-day period. After 2 hours of shearing, the average bubble radius $\langle R_b \rangle$ is reduced from 10 μm to about 1 μm . The average scale of the surface patterns $\langle r \rangle$ continues to increase during the early times of storage until it reaches a value of ~ 50 nm (Fig. 2B). The final bubble radii vary with the shear rate, with smaller bubbles being produced at higher shear rates. Nevertheless, the final pattern sizes are ~ 50 nm, independent of the bubble

size (Fig. 2C). Corresponding TEM images of the surface patterns when the bubble radii vary from 500 nm to 3 μm are shown in Fig. 2D. We also made dispersions using different surfactant mixtures with monoester content varying from 50 to 75 wt %. Over this composition range, the average bubble radius remains constant while the pattern size changes by a small amount (Fig. 2C).

The interface between air and liquid is covered with surfactant molecules, both mono- and

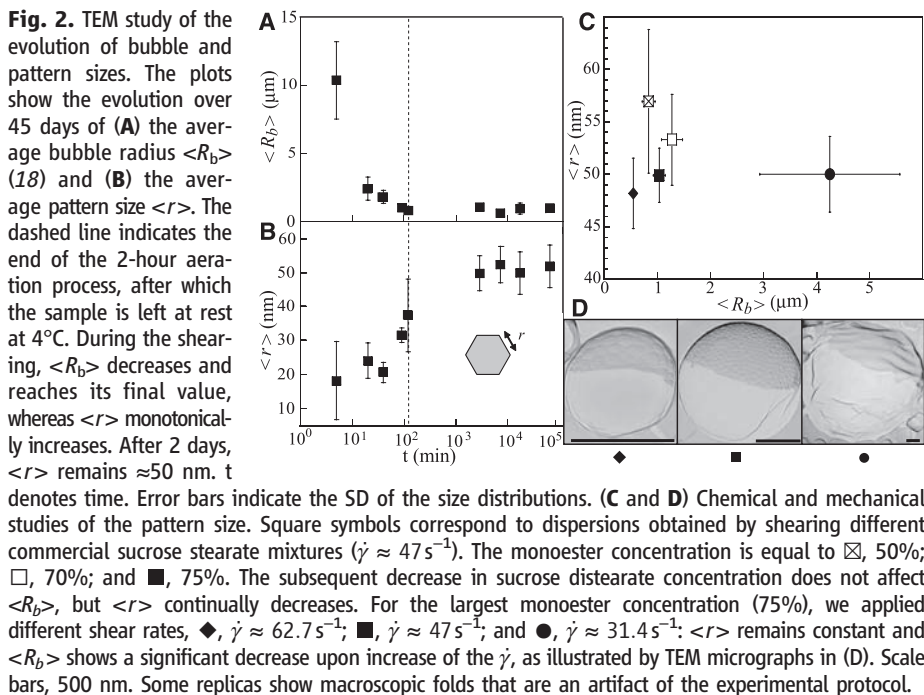
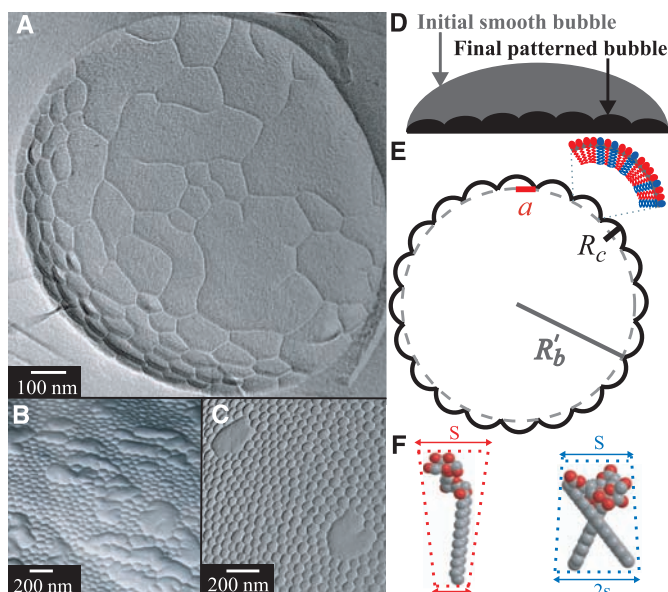


Fig. 3. Formation of the surface pattern. (A) TEM of a microbubble sampled after 20 min of aeration. The surface is not fully patterned but shows no isolated domains. Flat areas show short creases oriented away from existing patterns. (B) TEM image of a microbubble with nonpatterned areas, which, according to the shadowing, sit above the patterned areas. (C) TEM of a bubble prepared in a less viscous matrix (56 wt % glucose syrup). After the 2-hour aeration, flat areas remain. (D) Evolution from a smooth to a patterned surface. With a constant interfacial area, the buckling corresponds to a decrease in enclosed volume. (E) Schematic of the interfacial structure. The domains are modeled with spherical caps whose geometry (a , R_c) results from the packing of sucrose mono- and distearate (red and blue, respectively). (F) Structure of sucrose mono- and distearate (drawn using Chem 3D Ultra 9 software). At the interface, the molecules can be modeled by a truncated cone with a hydrophilic base or headgroup of surface area (S) and a hydrophobic base of surface area that is proportional to the number of C_{18} chains (s , monoester; $2s$, diester).



diesters, which are irreversibly pinned because of their low solubility in glucose syrup. The hydrophilic headgroups of the sucrose stearate sit in the aqueous phase, whereas the hydrophobic carbonyl chains lie inside the microbubbles. The observed bulging domains (Fig. 1B) suggest that the surfactant molecules pack on the interface, with headgroups occupying substantially more surface area than the hydrophobic chains. This interpretation is consistent with the disproportionation process that results in the shrinkage of the bubble and an increase of the interfacial density of surfactant molecules. At the end of the aeration process, the mono- and diester molecules form a highly ordered phase that is naturally bent away from the air phase.

An early stage of the pattern formation is shown in Fig. 3A. We did not observe individual condensed phase domains (17). This indicates that the polygonal shapes do not result from the compression or close packing of originally isolated structures. Instead, the smooth surface initially buckles in a few locations with creases that initiate domain boundaries growing at 120° ; the hexagonal patterning eventually covers the entire surface of the microbubbles (Fig. 3, A to C). Thus, the buckling is posterior to the interfacial condensation. As illustrated by Fig. 3B, the smooth regions (that is, the regions not yet covered with hexagons) project above the plane defined by the surrounding patterned area. The interfacial structuring is therefore associated with the reduction of the volume enclosed in a bubble of fixed surface area (Fig. 3D). This shrinkage of the microbubbles is consistent with Ostwald ripening, because these bubbles are the smallest ones of the dispersion. At room temperature, the conservation of the initial bubble surface area is due to the condensation of the interfacial layer and the irreversible pinning of the surfactant molecules.

More quantitatively, the surface state is considered to result from the thermodynamic evolution of an initially smooth, surfactant-covered interface. The domain size can be estimated by minimizing the energy of the microbubble upon shrinkage, driven by the Laplace pressure p . Each pattern is modeled as a spherical cap of radius R_c , which intersects the bubble surface with a circle of radius a (Fig. 3E). The total number of domains n , each of surface area A (a , R_c), is determined by conservation of the initial surface area of the bubble. We assume that the pattern geometry results from the energetic competition between the bending elasticity of the interface (bending rigidity κ), the formation of domain boundaries (line tension λ), and the normal pressure-volume work pV that accompanies shrinkage (19, 20):

$$E(a, R_c) = n \left(A \frac{\kappa}{2} \left(\frac{2}{R_c} - \frac{2}{R_{sp}} \right)^2 + \lambda \pi a \right) - pV \quad (1)$$

The bending rigidity of condensed monolayers is typically $\kappa \approx 200 k_B T$ (where k_B is the

Boltzmann constant and T the absolute temperature) $\approx 8.10^{-19}$ J (21). The spontaneous radius of curvature of the monolayer R_{sp} depends on the composition of the layer and the geometry of the surfactant molecules (22), which are modeled by truncated cones (Fig. 3F). The composition of the interface can be estimated from the presence of lamellae in nonaerated solutions of the same composition (fig. S3), which yields for the condensed phase the value of the packing parameter (23), the composition, and $R_{sp} \approx 80$ nm (SOM text). In addition, the line-tension energy is defined as the product of the line tension ($\lambda \approx k_B T l^{-1} \approx 2.10^{-12}$ J m^{-1} , where l is the length of the surfactant molecule) and the domain perimeter; the reduction by a factor of 2 in Eq. 1 arises because each boundary is shared by two domains. Finally, the pV term is approximated with the Laplace pressure on a micrometer-scale bubble with a surface tension $\gamma \approx 5 \times 10^{-4}$ J m^{-2} , which is on the order of the values measured for highly compressed monolayers such as pulmonary surfactants (24), so $p \approx 10^3$ Pa. The volume V of the buckled bubble is estimated as that of the spherical core ($V \approx \frac{4}{3} \pi R_b^3$) (Fig. 3E).

The energy minimization procedure for a bubble of $R_b = 1 \mu m$ leads to an estimate for the radius of the domains, $a \approx 40$ nm (SOM text), which lies within the range of the experimentally measured radii. The model also qualitatively captures the influence of the surfactant composition and bubble radius on the pattern size. For example, increasing the amount of diester in the initial mixture is expected to lead to an increased concentration of diester molecules at the gas/liquid interface, and therefore to a larger spontaneous radius of curvature. The model in

turn predicts larger pattern sizes (fig. S4). Similarly, the radius of the microbubble is expected to influence the number of patterns rather than their size (fig. S5), which is also consistent with the data (solid symbols in Fig. 2C). Finally, according to the experimental observations and to predictions of the model, the presence of patterns with increasing size during the preparation of the dispersion and the early time of the storage (Fig. 2B) can be rationalized either by evolution of the interfacial composition, which leads to changes in R_{sp} , or by changes in interfacial properties.

The time evolution of the distribution of bubble sizes has been characterized over 1 year, using SEM images (Fig. 4A) to estimate bubble radii (inset in Fig. 4A). The average bubble radius, R_b , increases from about 0.7 to 3.5 μm while the distribution broadens, with the standard deviation increasing by a factor of 10. These observations are consistent with destabilization by Ostwald ripening, which becomes significant only over long periods of time.

The shrinkage of the microbubbles is driven by the Laplace pressure due to the presence of narrow regions between domains that are hypothesized to be in a liquid state. Mass transfer of the gas can be characterized by a permeability or average speed of transport that, through the bulk phase around a bubble of $R_b \approx 1 \mu m$, is approximately $D/R_b \approx 10^{-5}$ $cm s^{-1}$, where the diffusion constant of air in glucose syrup D is estimated using the Stokes-Einstein relation (SOM text). The surfactant monolayer is expected to have a higher permeability (10^{-2} to 10^{-3} $cm s^{-1}$) (25) and therefore not limit the shrinkage. Thus, the time scale for the diffusion-controlled dissolution of micrometer-size bubbles in glu-

cose syrup is estimated to be about 5 hours [SOM text (13)], which is indeed the observed lifetime of SDS-coated microbubbles in glucose syrup but is orders of magnitude shorter than our observations (Fig. 4A). Therefore, reduced diffusion due to a viscous bulk phase cannot explain why the lifetime of microbubbles coated with mono- and diesters extends to more than a year.

Previous studies have shown that interfacial elasticity can stop or substantially reduce bubble dissolution (26, 27). In our system, the bending elasticity of the domains resists the compression of the interface upon shrinkage. Hence, we approximate the arrest of dissolution by diffusion as being when the bubble reaches a radius R at which the increase in bending energy away from the initial state balances the work of the Laplace pressure (SOM text): $\frac{R}{R_b} \approx 0.94$. This estimate shows that the buildup of elastic stress in the membrane arrests the shrinkage of the microbubbles very early and rationalizes the observed longevity of the dispersion.

According to the molecular model that we propose, the packing of the surfactant molecules controls the interfacial pattern structure and the stability of the bubbles. In order to test this idea further, we experimentally modified the composition of the original amphiphilic mixture by adding stearic acid. This surfactant molecule has a smaller headgroup, 0.2 nm^2 in water (28), but the same carbonyl chain, C_{18} , as the sucrose esters. When the acid concentration increases, the domains get larger ($a \approx 80$ nm for a stearic-acid concentration equal to 0.04 wt %) then lose their hexagonal shape, and finally disappear as the surface of the bubble becomes smooth (Fig. 4, B to E). Upon addition of stearic acid, the average headgroup size of the surfactant mixture decreases, which is expected to result in an increase of R_{sp} . The thermodynamic model predicts an increase in pattern size, which is consistent with our observations (Fig. 4, B to E, and fig. S4).

Our preparation and long-term study of microbubbles in a viscous continuous phase demonstrate that it is possible to achieve stabilization of such a dispersion for more than 1 year. The observed regular surface patterning is the thermodynamic signature of the formation of an elastic, condensed surfactant phase, which also correlates with the extended stability of the system. The nanometer-scale features can be tuned by modification of the chemical composition of the interface. Beyond the experimental observations reported here, our approach will be useful for designing more complex surfaces by controlling the self-assembly of the surfactant and for studying the behavior of individual stable bubbles of colloidal dimensions.

References and Notes

1. D. Myers, *Surfaces, Interfaces and Colloids* (Wiley-VCH, New York, 1999).
2. R. G. Larson, *The Structure and Rheology of Complex Fluids* (Oxford Univ. Press, Oxford, 1999).
3. M. Wang, J. Wang, N. Pan, S. Chen, J. He, *J. Phys. D Appl. Phys.* **40**, 260 (2007).

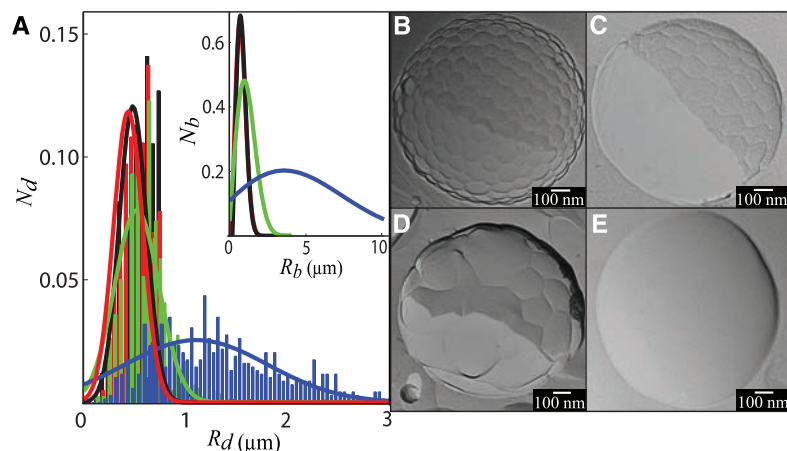


Fig. 4. Stability of microbubbles and chemical modification of surface patterns. **(A)** Evolution of distributions of microbubble radii over 1 year. For each histogram, we used SEM images to measure the radii of about 800 disks (R_d), which are the intersections of the bubbles with the plane along which the sample has been fractured. N_d is the fraction of bubbles that intersect the plane with a radius R_d , which is less than or equal to the actual radius of the bubble (R_b). These distributions are fitted with Gaussian curves, which are used to extrapolate the distributions of the radii (R_b) of the bubbles (inset) (29). N_b is the fraction of bubbles with radius R_b . Samples of different ages were studied: 2 days (red), 1 week (black), 4 months (green), and 1 year (blue). The distributions show a modest shift and broadening over time. **(B to E)** Evolution of pattern structure upon addition of stearic acid. The TEM micrographs correspond to 1-week-old samples prepared by addition of (B) 0 wt %, (C) 0.04 wt %, (D) 0.08 wt %, and (E) 0.2 wt % of stearic acid. The pattern evolves, first showing a size increase (C), then losing the regularity (D), before disappearing (E).

4. S. Subramonian, L. Remy, D. Schroer, *Cell. Polym.* **23**, 349 (2004).
5. S. Hilgenfeldt, S. A. Koehler, H. A. Stone, *Phys. Rev. Lett.* **86**, 4704 (2001).
6. R. D. MacPherson, D. J. Srolovitz, *Nature* **446**, 1053 (2007).
7. K. Stratford, R. Adhikari, I. Pagonabarraga, J. C. Desplat, M. E. Cates, *Science* **309**, 2198 (2005).
8. M. Abkarian *et al.*, *Phys. Rev. Lett.* **99**, 188301 (2007).
9. S. H. Bloch, R. E. Short, K. W. Ferrara, E. R. Wisner, *Ultrasound Med. Biol.* **31**, 439 (2005).
10. S. Cohen-Addad, H. Hoballah, R. Hohler, *Phys. Rev. E Stat. Phys. Plasmas Fluids Relat. Interdiscip. Topics* **57**, 6897 (1998).
11. O. Faruk, A. K. Bledzki, L. M. Matuana, *Macromol. Mater. Eng.* **292**, 113 (2007).
12. P. S. Epstein, M. S. Plesset, *J. Chem. Phys.* **18**, 1505 (1950).
13. P. B. Duncan, D. Needham, *Langmuir* **20**, 2567 (2004).
14. E. Dickinson, R. Ettelaie, T. Kostakis, B. Murray, *Langmuir* **20**, 8517 (2004).
15. D. H. Kim, M. J. Costello, P. B. Duncan, D. Needham, *Langmuir* **19**, 8455 (2003).
16. E. Talu, M. M. Lozano, R. L. Powell, P. A. Dayton, M. L. Longo, *Langmuir* **22**, 9487 (2006).
17. M. A. Borden *et al.*, *Langmuir* **22**, 4291 (2006).
18. Materials and methods are available as supporting material on Science Online.
19. T. Baumgart, S. T. Hess, W. W. Webb, *Nature* **425**, 821 (2003).
20. H. Diamant, T. A. Witten, A. Gopal, K. Y. C. Lee, *Europhys. Lett.* **52**, 171 (2000).
21. J. Daillant, J. J. Benattar, L. Bosio, *J. Phys. Condens. Matter* **2**, 405 (1990).
22. G. Garofalakis, B. S. Murray, *Langmuir* **18**, 4765 (2002).
23. J. N. Israelachvili, *Intermolecular and Surface Forces* (Academic Press, New York, 1992).
24. L. M. Y. Yu *et al.*, *J. Appl. Physiol.* **97**, 704 (2004).
25. M. A. Borden, M. L. Longo, *J. Phys. Chem. B* **108**, 6009 (2004).
26. W. Kloeck, T. Van Vliet, M. Meinders, *J. Colloid Interface Sci.* **237**, 158 (2001).
27. A. R. Cox, F. Cagnol, A. B. Russell, M. K. Izzard, *Langmuir* **23**, 7995 (2007).
28. Y. Wang, X. Du, L. Guo, H. Liu, *J. Chem. Phys.* **124**, 134706 (2006).
29. S. F. Edwards, D. R. Wilkinson, *J. Phys. D Appl. Phys.* **13**, 209 (1980).
30. The authors acknowledge the following individuals for preliminary work: Industrial training students from the University of Wageningen ran the first aeration experiments at Unilever Research (Colworth, UK); M. Fitzgerald from the University of Reading, UK, and S. Brockbank from the University of Bristol, UK, studied the surfactant mixtures during their Ph.D. studies. We thank A. Weaver, J. Brigham, M. Kirkland, and T. Belmar of Unilever Research; R. Schaleck and E. Hodges of Center for Nanoscale Systems at Harvard University; B. Graham and A. Graham of Bibs Lab for their help with the imaging; M. Brenner, L. Courbin, J. Hutchinson, J. Lucassen, and D. Weitz for helpful conversations; and Unilever Research for support of this work.

Supporting Online Material

www.sciencemag.org/cgi/content/full/320/5880/1198/DC1

Materials and Methods

SOM Text

Figs. S1 to S5

References

26 December 2007; accepted 25 April 2008

10.1126/science.1154601

The Sensitivity of Polar Ozone Depletion to Proposed Geoengineering Schemes

Simone Tilmes,^{1*} Rolf Müller,² Ross Salawitch³

The large burden of sulfate aerosols injected into the stratosphere by the eruption of Mount Pinatubo in 1991 cooled Earth and enhanced the destruction of polar ozone in the subsequent few years. The continuous injection of sulfur into the stratosphere has been suggested as a “geoengineering” scheme to counteract global warming. We use an empirical relationship between ozone depletion and chlorine activation to estimate how this approach might influence polar ozone. An injection of sulfur large enough to compensate for surface warming caused by the doubling of atmospheric CO₂ would strongly increase the extent of Arctic ozone depletion during the present century for cold winters and would cause a considerable delay, between 30 and 70 years, in the expected recovery of the Antarctic ozone hole.

Geoengineering schemes have been proposed to alleviate the consequences of global warming (1–3) by continuous injection of sulfur into the stratosphere. Volcanic eruptions in the past have shown that strongly enhanced sulfate aerosols in the stratosphere result in a higher planetary albedo, leading to surface cooling (4). On the other hand, the potential for exceedingly high Arctic ozone depletion resulting from the simultaneous presence of high surface area density (SAD) of sulfate aerosols and cold conditions in the polar stratosphere is known (5, 6) but was not quantified in the context of geoengineering (1–3).

In this report, the impact of enhanced sulfate aerosol (due to geoengineering) on future chemical polar ozone depletion is quantified. Our analysis is based on the past dependence of ozone loss on aerosol content derived via the combina-

tion of a model and measurement for both the Antarctic and Arctic and by taking into account the expected future stratospheric halogen loading. We describe this dependence by the empirical relation between observed chemical ozone loss and the potential for the activation of chlorine (PACl). PACl accounts for year-to-year variations in temperature, sulfur burden, and the halogen content of the stratosphere. This relation is shown to be valid based on past observations, including 4 years of volcanically enhanced aerosol loading in the stratosphere.

Severe chemical loss of ozone over the Arctic and Antarctica is caused by anthropogenic halogens. The combination of very low temperatures and increasing sunlight after the polar night results in a strong transformation of chlorine from reservoir forms to reactive radicals, leading to the rapid destruction of polar ozone (7). Since the 1990s, most of the available ozone has been destroyed in the Antarctic lower stratosphere (between 12 and 20 km in altitude), which corresponds to a loss in column ozone of about 120 to 150 DU (or Dobson units, one of which

equals 2.687×10^{16} molecules per cm²) (8). In the Arctic, the interannual variability of temperatures, and therefore of ozone depletion, is much larger. Chemical depletion of ozone in recent cold Arctic winters exceeded 100 DU [see the supporting online material (SOM)] (8–11). Over the next half-century, the stratospheric halogen loading—commonly quantified by a measure referred to as Effective Equivalent Stratospheric Chlorine (EESC)—is projected to slowly decline (12). Close to the year 2070, EESC is predicted to reach values last seen in 1980, a benchmark for the recovery of polar ozone (12, 13). Our work is motivated by the concern that elevated SAD attributable to geoengineering will lead to additional ozone depletion that may delay the recovery of polar ozone.

We demonstrate the importance of chlorine activation on cold, liquid sulfate aerosols for polar ozone depletion by comparing two relations between chemical ozone loss and chlorine activation based on past observations (Fig. 1). The first relation is based on a previous description of polar chlorine activation: the polar stratospheric cloud (PSC) formation potential or PFP (8). PFP describes the fraction of the polar region that is below the threshold temperature for existence of PSCs (T_{PSC}). For cold Arctic winters, more than 10% of the vortex region is cold enough to support PSCs, whereas for warm winters, PFP is close to zero. The derived linear relation is compact, except for values derived for the four winters after the eruption of Mount Pinatubo in June 1991.

The second relation (Fig. 1B) accounts additionally for stratospheric aerosol loading. Tilmes *et al.* (14) defined the potential for the activation of chlorine, which is similar to PFP but uses a threshold temperature for chlorine activation (T_{ACl}) as described by Drdla (15). A description of the calculation of this temperature can be found in (14), which is a function of temperature, ambient H₂O, and SAD. For background levels of SAD (e.g., an atmosphere not perturbed by large volcanic eruptions) and present-day values of EESC, PACl is comparable to PFP. After a strong

¹National Center for Atmospheric Research (NCAR), Boulder, CO 80307, USA. ²Research Center Jülich, 52425 Jülich, Germany. ³University of Maryland, College Park, MD 20742, USA.

*To whom correspondence should be addressed. E-mail: tilmes@ucar.edu